Arctic Air Masses in a Warming World

MELISSA GERVAIS, EYAD ATALLAH, JOHN R. GYAKUM, AND L. BRUNO TREMBLAY

Department of Atmospheric and Oceanic Science, McGill University, Montreal, Quebec, Canada

(Manuscript received 10 July 2015, in final form 8 December 2015)

ABSTRACT

An important aspect of understanding the impacts of climate change on society is determining how the distribution of weather regimes will change. Arctic amplification results in greater warming over the Arctic compared to the midlatitudes, and this study examines how patterns of Arctic air masses will be affected. The authors employ the Community Earth System Model Large Ensemble (CESM-LE) RCP 8.5, consisting of 30 ensemble members run through the twenty-first century. Self-organizing maps are used to define archetypes of 850-hPa equivalent potential temperature θ_{e850} anomalies with respect to a changing climate and assess changes in their frequency of occurrence. In the model, a pattern with negative θ_{e850} anomalies over the central Arctic becomes less frequent in the future. There is also an increase in the frequency of patterns associated with an amplified ridge (trough) with positive (negative) θ_{e850} anomalies over western (eastern) North America. It is hypothesized that the increase in frequency of such patterns is the result of enhanced forcing of baroclinic waves owing to reduced sea ice over the western Arctic. There is also a decline in patterns that have anomalously high θ_{e850} over the North Atlantic, a pattern that is associated with intense ridging in the 500-hPa flow over the North Atlantic and colder θ_{e850} over Europe. The authors relate the decrease of these patterns to an enhancement of the North Atlantic jet induced by a warming deficit in the North Atlantic Ocean.

1. Introduction

With global climate change, both historical observations (Serreze et al. 2008; Screen and Simmonds 2010) and future climate modeling studies (Holland and Bitz 2003; Kay et al. 2012) predict a rise in global temperature that is larger over the Arctic than the midlatitudes, known as Arctic amplification. However, society is not only concerned with the average future climate change but also how this will be manifested as the daily weather people experience. Will regimes of cold temperatures over the northeastern United States and eastern Canada that typified the winters of 2013/14 and 2014/15 become more common in the future? Can we expect a cold European winter pattern similar to that of 2012/13 to occur more often in the future? These questions cannot be addressed through an examination of the average change in temperature. They require an understanding of the variability of airmass patterns and how these will change in the future. Of particular importance is the formation of Arctic air masses and their associated changes in the midlatitude flow.

Arctic or polar continental air masses are cold and dry air masses generally associated with deep and persistent near-surface temperature inversions (Curry 1983). These inversions are the result of effective radiative cooling over highly emissive snow and sea ice covered surfaces and are enhanced because of radiative cooling from ice crystals through the depth of the column (Curry 1983). In general, the maximum cooling for the formation of Arctic air masses occurs over land as a result of ocean heat conduction through sea ice (Curry 1983). These air masses can be advected into the midlatitudes to create cold air outbreaks (Walsh et al. 2001). For example, Walsh et al. (2001) demonstrated that cold air masses in midlatitude North America originate from northern Canada, the central Arctic, or Asia.

The observed (Serreze et al. 2008) and predicted (Kay et al. 2012) vertical structure of Arctic amplification has the largest increases in temperature at the surface and decreased warming with height. Therefore, polar amplification implies a reduction in the strength of surface inversions typical of Arctic air masses. There are several positive feedbacks responsible for Arctic amplification, the most important being surface albedo and lapse rate

Corresponding author address: Melissa Gervais, Department of Atmospheric and Oceanic Science, McGill University, 805 Sherbrooke Street West, Montreal QC H3A 0B9, Canada.
E-mail: melissa.gervais@mail.mcgill.ca

DOI: 10.1175/JCLI-D-15-0499.1

feedbacks (Pithan and Mauritsen 2014; Graversen et al. 2014). As the fraction of surface area covered by highly reflective sea ice and snow declines, they are replaced by open ocean and land with a lower albedo, resulting in enhanced absorption of heat at the surface and thus more melting (Manabe and Wetherald 1975). The positive lapse rate feedback in the atmosphere is caused by the existence of a surface temperature inversion, which confines the Arctic warming to the lower levels (Manabe and Wetherald 1975) and requires a larger surface warming to balance changes in radiation at the top of the atmosphere (Pithan and Mauritsen 2014).

The goal of this work is to expand upon our understanding of climatological changes in Arctic air masses owing to Arctic amplification and examine how their variability may change in the future. To address this problem, we employ a 30-member ensemble of future projections from the Community Earth System Model (CESM) Large Ensemble (CESM-LE) fully coupled model. This new large ensemble allows us to examine changes in the internal variability of airmass patterns, providing the equivalent of 30 yr of climatological variability for each model year. To represent Arctic air masses, we use the January–February (JF) equivalent potential temperature field at 850 hPa (θ_{e850}) north of 50°N, a measure of both temperature and moisture. To identify relevant patterns, we use a self-organizing maps technique, which allows us to both identify archetypes of θ_{e850} anomaly patterns and examine how their frequency of occurrence changes through time. The combination of the large-ensemble data and the self-organizing maps method allows us to separate out the forced climate change signal from changes in internal variability. This allows us to answer the question of how patterns of air masses will change in the future. Furthermore, there will be implications on flow regimes, such as the Arctic Oscillation and midlatitude planetary waves, which may impact the formation and movement of these air masses and are likely to experience changes in the future.

2. Data and methods

a. Data

This study utilizes data from the CESM Large Ensemble RCP8.5 for 2006–80, consisting of 30 ensemble members (Kay et al. 2014). Each ensemble member represents a realization of the future climate, and together the 30 members provide a wide range of potential solutions that differ only because of internal variability of the climate system. This is an advantage over multimodel ensembles, where different physics are represented in addition to internal variability. Details regarding the CESM-LE experiment can be found in Kay et al. (2014).

The CESM is the most recent version of the National Center for Atmospheric Research's global coupled model comprised of four component models: the Community Atmosphere Model 5 (CAM5); the Parallel Ocean Program, version 2, (POP2); the Community Ice Code (CICE4); and the Community Land Model, version 4 (CLM4) (Hurrell et al. 2013). The component models are identical to the previous model version, the Community Climate System Model, version 4, (CCSM4) (Gent et al. 2011), except for the atmospheric component (Hurrell et al. 2013). CAM5 has undergone several improvements from the previous version, CAM4, including increased vertical resolution from 26 to 30 levels, new parameterization schemes for moist turbulence and shallow convection, and changes to the cloud microphysics scheme (Neale et al. 2012). Of significance for the Arctic are the resulting improvements in the representation of the total cloud percentage (Barton et al. 2012; Kay et al. 2012).

A comprehensive analysis of the representation of the Arctic in CESM has yet to be conducted as it was by De Boer et al. (2012) for CCSM4. De Boer et al. (2012) found that CCSM4 generally represents the patterns of surface air temperature with a small negative bias on the order of −2 K. They do find a significant negative bias in sea level pressure (SLP) over the Arctic, resulting in a weaker Beaufort high than is observed (De Boer et al. 2012). This influences the Beaufort Gyre, leading to errors in sea ice motion (Jahn et al. 2012). Otherwise, the Arctic sea ice in CCSM4 compares well with observed sea ice in terms of concentration and thickness (Jahn et al. 2012). The negative SLP bias over the Arctic is corrected in CESM; however, there are still issues with the Beaufort high being situated closer to the Eurasian coast than in the observations (DeRepentigny et al. 2015, manuscript submitted to *J. Climate*). CESM has a similarly well-simulated Arctic sea ice cover but experiences more rapid sea ice loss than the previous model version, presumably as a result of improvements to the cloud parameterizations and their resulting improvement of Arctic surface temperature (A. Jahn 2014, personal communication).

In this study, Arctic air masses are represented by patterns of θ_{e850} north of 50°N. Here, θ_{e850} is the temperature an air mass would have if it were lifted to the lifting condensation level, condensing out all of its moisture, and compressed adiabatically to a reference pressure (1000 hPa) (Holton 2004, p. 290). As such, it is conserved under adiabatic motion. It is a good metric for air masses since it integrates both temperature and specific humidity, which are used to distinguish between airmass types. The number of vertical levels that are archived in the CESM-LE is limited, so θ_{e850} is estimated using a simplified form (Holton 2004, p. 291) as follows:

$$\theta_e = T\left(\frac{P_0}{P}\right)^{R/c_{pd}} \exp\left(\frac{L_c}{c_{pd}T}\frac{q}{1-q}\right), \quad (1)$$

where T is temperature (K) at 850 hPa, $P = 850$ hPa, q is specific humidity, the latent heat of condensation $L_c = 2.5 \times 10^6\,\mathrm{J\,kg^{-1}}$, the specific heat for dry air at constant pressure $c_{pd} = 1004\,\mathrm{J\,kg^{-1}\,K^{-1}}$, the specific gas content $R = 287.04\,\mathrm{J\,kg^{-1}\,K^{-1}}$, and the reference pressure $P_0 = 1000$ hPa. All analysis is conducted for the months of January–February, when Arctic temperatures are coldest on average.

b. Self-organizing map algorithm

The self-organizing map algorithm uses competitive machine learning to represent the probability density function of a dataset using a two-dimensional grid of map nodes. The method allows for the classification of large volumes of data into a predetermined number of archetypes that are organized based on their similarities. Since its introduction by Kohonen (1982), the self-organizing map (SOM) algorithm has been applied in a variety of different disciplines and is gaining popularity in the atmospheric sciences (Huth et al. 2008). It has been used to investigate synoptic circulations associated with extreme events, as in E. N. Cassano et al. (2006), a study of extreme temperature and winds in Barrow, Alaska, and Cavazos (2000), which examined extreme precipitation in northeastern Mexico/southeastern Texas. The SOM algorithm can also be used as a novel method for the validation of model variability, through comparison between observation and model SOM node frequencies (Schuenemann and Cassano 2009). In a climate change context, the method has also been applied to demonstrate changes in patterns and variability in global climate models (GCMs) run with future climate scenarios (Schuenemann and Cassano 2010; J. J. Cassano et al. 2006). An extended discussion on the application of SOMs for synoptic climatology can be found in Hewitson and Crane (2002).

The SOM algorithm is an iterative process by which input data are used to train a SOM that represents the data's distribution. The input data are first normalized, then multiplied by the cosine of the latitude to take into account the variation in gridbox size with latitude. This way grid boxes with smaller area or greater variance do not have a disproportionately larger influence on the analysis. The user defines a SOM size that determines the number of map nodes or patterns to represent the data. For example, the final SOM size chosen for this study (after sensitivity testing) is 3×4, giving a total of 12 nodes. The SOM nodes are then initialized with random data prior to node training.

The SOM training algorithm proceeds by repeated comparison of input data vectors to the SOM nodes. For example, the data vectors in this study are daily maps of θ_{e850}. A best match unit m_i is determined to be the map node that has the smallest Euclidean distance to the input data vector $\mathbf{x}_i$. The best match unit and surrounding nodes are then updated as follows:

$$m_i(t+1) = m_i(t) + \alpha(t)h_{ci}(t)[\mathbf{x}(t) - m_i(t)], \quad (2)$$

where t is the training time, α is the learning rate parameter, and h_{ci} is the neighborhood function. The learning rate parameter defines the amount by which the map is updated, which in this study is an inverse function of training time (Vesanto et al. 2000; Kohonen 2001, p. 145). The neighborhood function h_{ci} represents the shape of the influence. There are several commonly applied neighborhood functions. Here we use the Epanechikov function, which was shown by Liu et al. (2006) to outperform other common radius functions in simplified tests. The Epanechikov function is

$$h_{ci} = \max\left(0, 1 - \frac{d^2}{r^2}\right). \quad (3)$$

The map distance to the best match unit is d, where adjacent map nodes have a distance of 1. The radius of influence r is the maximum distance away from the best match unit where the input data still have influence. The shape of h_{ci} is maximized at the best match unit and decreases to zero at the radius of influence. It is good practice to begin the training with a radius of influence equal to the diameter of the SOM to ensure that all nodes are updated and decrease the value with training time (Kohonen 2001). The SOM may be trained in multiple training steps, and it proceeds for some multiple of the total number of data vectors, which in this study is the total number of days. Further details on the SOM algorithm can be found in Kohonen (2001), and software are freely available (Vesanto et al. 2000; http://www.cis.hut.fi/research/som-research/).

The greatest advantage of using SOMs over the more traditional analysis of empirical orthogonal functions (EOFs) is the lack of restrictions of orthogonality and stationarity of identified patterns. Processes in the atmosphere are not always well represented by orthogonal patterns, such as the θ_{e850} anomaly field, where the first EOF represents only 7% of the variability. The use of a SOM can identify sets of nonorthogonal patterns in data that may be more physically relevant, which Liu et al. (2006) demonstrated in an idealized setting using a repeating set of nonorthogonal one-dimensional patterns. An EOF of these data produced one of the predefined patterns as the first EOF and a mixture of the other patterns as the second EOF. A SOM of the same data reproduced all four patterns. This blending of patterns,

owing to the orthogonality constraint, has also been shown in two dimensions, both in an idealized setting (Reusch et al. 2005) and as applied to variability in the North Atlantic (Reusch et al. 2007).

Another issue that can compromise the utility of an EOF analysis is the impact of changing atmospheric patterns in time. Tremblay (2001) conducted an idealized study of the North Atlantic Oscillation (NAO) with a shift in the northern center of action, similar to the regime shift in the mid-1970s. The results of this study showed a first EOF that was a north–south-oriented dipole, consistent with the NAO, and a second EOF that was an east–west dipole. This study demonstrates that nonstationarity in atmospheric patterns can result in the generation of nonphysical EOF modes. In contrast, Johnson et al. (2008) were able to identify the shift in centers of action of the NAO with time using SOMs. The SOM in Johnson et al. (2008) identified both NAO patterns that were north–south oriented and ones with patterns where the northern center of action was shifted to the east. They also demonstrated the shift between the two as relative changes in the frequency of occurrence of these patterns. This is an important implication to consider when conducting analysis of atmospheric fields in a changing climate.

In comparison to other clustering methods, a useful trait of the SOM is the organization of the SOM with more similar patterns being closer together. This is a product of the neighborhood function, which alters not just the winning map node but also the nodes within a given distance from the winning node. If the radius of influence in the neighborhood function were always one, there would be no topological ordering in the SOM, and thus the SOM would be reduced to an adaptive *K*-means clustering method, as described in Murtagh and Hernández-Pajares (1995).

Although SOMs present several advantages over traditional methods, a drawback to the method is the large number of free parameters involved, which can lead to some subjectivity in producing a SOM. The size of the SOM is user defined and chosen so as to represent the distribution required for the study with the fewest patterns. Depending on the problem being studied, the SOM size could impact the patterns identified. In this study, increasing the size of the SOM resulted in the duplication of preexisting patterns, indicating that the SOMs are robust with respect to size in their identification of important patterns.

There are also several tunable parameters within the algorithm itself, such as the learning rate function, training length, and radius of influence. We conduct tests of these free parameters and choose SOMs based on measures of the quality of the SOM produced. The Sammon mapping algorithm (Sammon 1969) is a nonlinear mapping from higher to lower dimension, which represents the Euclidean distance between the map nodes onto a two-dimensional field. Using this method, a Sammon map can be generated to determine the topology or spatial relationship between map nodes. This provides information about how similar map nodes are to one another. A well-constructed SOM should have a flat Sammon map, where the ordering of the map nodes is preserved (Kohonen 2001). The quantization error (QE) is a measure of how similar the data are to the best match unit and is the average Euclidean distance between a data vector and its best match unit (Vesanto et al. 2000). The topographic error (TE) is the percentage of data vectors for which the second-best match node is not adjacent to the winning node and is a measure of how well ordered the SOM is (Vesanto et al. 2000). W. Gutowski (2015, personal communication) has shown that, during the training of a SOM overfitting of the SOM can result in lower QE at the expense of higher TE. In the creation of SOMs in this study, the free parameters are chosen so that the resulting SOM has a balance of low QE, low TE, and a well-ordered Sammon map. In such well-constructed SOMs, we find that the general patterns identified by the SOMs are robust regardless of the tunable parameters chosen (not shown).

c. Creation of a master SOM

In this study, we are interested not only in the mean change in Arctic air masses, but also in how the internal variability will change in the future. To isolate these changes in internal variability, we leverage the large number of ensembles to create a daily θ_{e850} anomaly field with respect to the changing climate. An annual JF ensemble average field is created to represent the changing climate. There are small year-to-year differences in the annual JF ensemble averages, indicating that internal variability has some remaining impact, even with the large ensemble. The anomaly field is computed as the daily θ_{e850} values minus the annual JF ensemble average, repeated for all years and ensemble members. A 3×4 master SOM is created using these daily θ_{e850} anomalies (Fig. 1). Tests with larger SOM sizes revealed qualitatively similar patterns to the 3×4 but more duplicate patterns, and a reduction in the SOM size lead to the merging of patterns. Consequently, a 3×4 SOM was chosen so as to balance the need to fully represent the distribution of atmospheric patterns with the least number of maps possible.

Two sets of trainings are employed in the generation of the master SOM, the training length for each being 10 times the number of days of input data. With this training length, there is a balance between QE and TE,

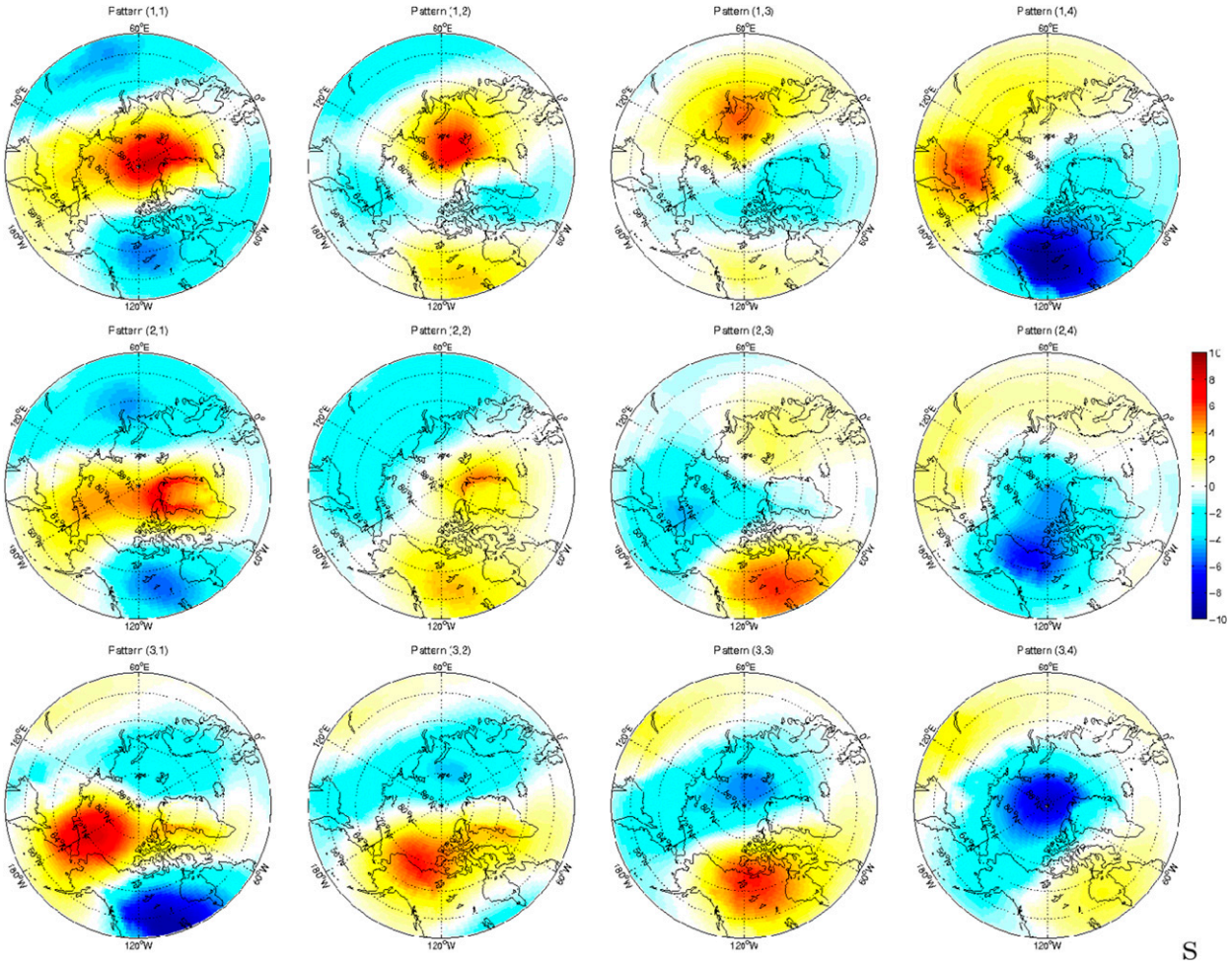

FIG. 1. Map node patterns for master SOM of daily θ_{e850} anomalies with respect to annual JF ensemble mean (K; color).

and both are adequately small (not shown). The first and second trainings, respectively, have radii of influence of 6 and 2 and alpha values of 0.5 and 0.1. The Sammon map is well ordered with generally equal distances between map nodes (Fig. 2). These measures of SOM quality demonstrate that the master SOM is well constructed.

3. Results

a. Climatological change

The development of the CESM Large Ensemble provides the range of internal variability that is necessary to produce a climatology over a short time period (Kay et al. 2014). Here we conduct ensemble averages of two decades (2010–20 and 2070–80) to investigate how the climatology changes from the beginning to the end of the study period. For θ_{e850}, we see an expected Arctic amplification signal of higher θ_{e850} over the entire central Arctic Ocean (on the order of 5 K) and smaller increases over the midlatitudes (Fig. 3). In general, the greatest increases in θ_{e850} occur in regions that are initially the coldest. This results in greater increases in θ_{e850} in the northeast of the continents, acting to weaken the preexisting east–west θ_{e850} gradient.

Accompanying these increases in θ_{e850} are climatological changes in related mass fields. The 500-hPa geopotential height Z_{500} increases over the central Arctic and Eurasia (Fig. 4a) by the end of the time period, with a pattern similar to the θ_{e850} increases (Fig. 3). This is to be expected with a general warming throughout the troposphere. Over the North Atlantic, where the θ_{e850} anomaly was smallest (Fig. 3), there is also a deficit in Z_{500} height increases (Fig. 4a). On the equatorward edge of this deficit in Z_{500} increases, we see an enhanced 200-hPa wind speeds V_{200} up to 4 m s^{-1}, an increase on the order of 10% (Fig. 4a). This is indicative of a strengthening and eastward extension of the North Atlantic jet in the future (not shown), which Simpson et al. (2014) find to be a robust feature between various CMIP5 models.

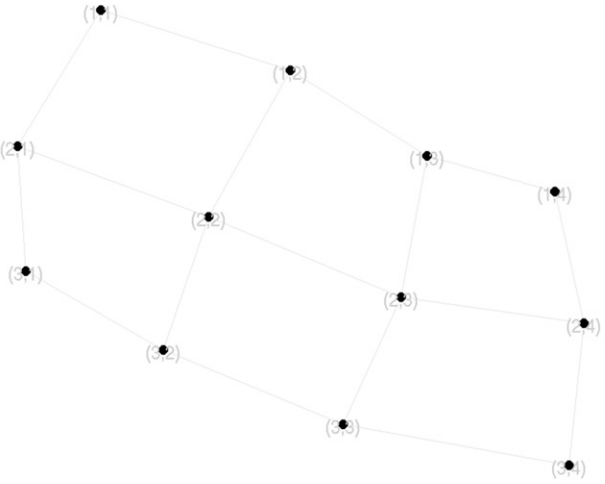

FIG. 2. Sammon map representing the relative Euclidean distances between the map nodes for the SOM shown in Fig. 1.

There are also climatological changes in the low-level (850 hPa) relative vorticity (Fig. 4b). In the Pacific, there is a region of anomalous cyclonic vorticity over the Bering Sea and anticyclonic anomalies to the south across the western central Pacific. A cyclonic vorticity anomaly is also present over the Greenland, Iceland, and Norwegian Seas, with a region of anticyclonic anomalies over Europe.

At the surface, the climatological difference in mean sea level pressure between the 2070–80 and 2010–20 climatologies reveals a decline in SLP over the eastern Arctic (Barents/Kara Seas), western Arctic (Bering/Chukchi Seas), Sea of Okhotsk, and Hudson Bay (Fig. 4c). Commensurate with these regions of low pressure are enhanced turbulent heat fluxes and declines in sea ice concentration (SIC) (Fig. 4d). This is suggestive of a link between sea ice and local SLP.

In the North Atlantic there is a relative cooling in SSTs (Fig. 4e) consistent with the North Atlantic "warming hole" discussed in Drijfhout et al. (2012). Above this warming hole region, there is a decrease in turbulent heat flux and smaller increase in θ_{e850} and Z_{500} heights relative to surrounding regions (Figs. 3, 4a). These changes in SST and SIC may represent important changes in the surface topography with dynamic and thermodynamic impacts on the overlying atmosphere, which will be further examined in the discussion section.

b. Internal variability

The master SOM of θ_{e850} anomalies identifies dominant airmass patterns relative to a changing climatology (Fig. 1). Pattern (3,4) has lower (higher) θ_{e850} over the central Arctic (midlatitudes), which we will refer to as the cold Arctic node. There are higher θ_{e850} anomalies over northern North America in nodes (2,2), (2,3), (3,2), and (3,3), which we will refer to as warm North American Arctic nodes, and lower θ_{e850} over northern North America in nodes (1,4), (2,4), and (3,1), which we will refer to as cold North American Arctic nodes. Nodes (1,1), (2,1), and (1,2) have higher (lower) θ_{e850} over the eastern/central Arctic (central Russia/Europe), which we will refer to as warm eastern Arctic nodes.

The occurrence of these patterns and their change in time are investigated by computing time series of best match unit frequency (BMUF) per year for each map node. The internal variability of pattern frequency is provided by the large number of ensemble members. The substantial spread between the median, quartiles, and extrema of BMUF across ensemble members demonstrates the large internal variability (Fig. 5).

The self-organizing maps methodology assumes a data distribution that is a continuum such that if there are members that are very different from one another and there are no observed patterns in between, a transitional SOM node could be generated but rarely be the best match unit. In this master SOM, all members are representative of patterns at some point in the time period, and the frequencies are generally well distributed, with no member grossly outweighing the rest in terms of frequency of occurrence (Fig. 5). With a 12-node SOM, a frequency of 8.33% for each node would represent an equal distribution across the map nodes.

The frequency of occurrence of these nodes is changing throughout the time period (Fig. 5). Multiple linear regression applied to the BMUF of each SOM node reveals statistically significant trends at the 95th percentile in several of the map nodes. In particular, the cold Arctic node (3,4) and two of the warm eastern Arctic nodes [(1,1) and (2,1)] are decreasing in frequency in the future. The cold North American Arctic patterns on the right side of the SOM [(1,4) and (2,4)] are increasing in frequency, as well as three of the warm North American Arctic patterns [(2,2), (2,3), and (3,2)].

The associated mass fields with each of these SOM nodes can be used to gain further understanding of the processes involved in generating differing θ_{e850} patterns. To this end, SOM node composites are computed for each of the map nodes by averaging days when the map node is the best match unit. Since many of the mass fields experience large changes throughout the time period, we show these results for the node composites of the 2070–80 time period. Figure 6 shows the composites of SLP, 500-hPa heights, and θ_{e850} anomalies for each of the SOM nodes, and Fig. 7 does the same for anomalies

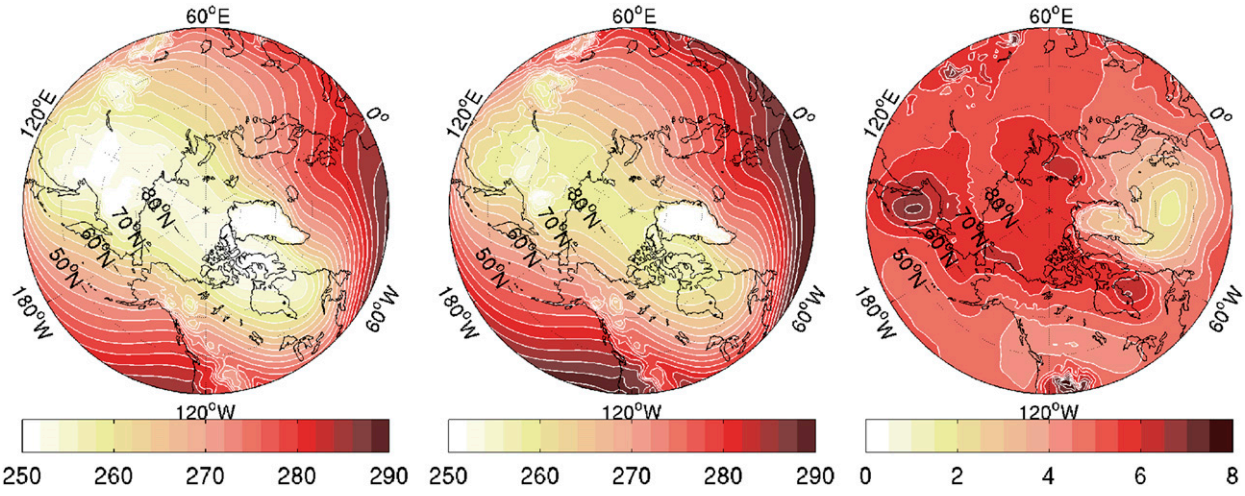

FIG. 3. Decadal JF ensemble-mean θ_{e850} (K) for (left) 2010–20, (middle) 2070–80, and (right) difference (2070–80 minus 2010–2020).

in SLP and SIC. For the fields shown in this study, the magnitudes of the variability differ depending on the decade of study chosen, but the patterns are similar between decades (not shown).

The cold Arctic node (3,4) is associated with lower SLP and 500-hPa height, as well as more zonal geostrophic upper-level flow centered over the Arctic (Figs. 6, 7). These features are indicative of a well-developed polar vortex and are typically associated with a positive Arctic Oscillation (AO). This node is also experiencing some of the largest trends in its frequency of occurrence at -5% century^{-1} (Fig. 5).

The warm North American Arctic nodes [(2,2), (2,3), (3,2), and (3,3)] all have a ridge over western North America with higher θ_{e850} anomalies centered on the ridge axis (Fig. 6). Node (2,2) has a moderately amplified ridge, with positive θ_{e850} anomalies across North America and negative θ_{e850} anomalies over Eurasia. Node (3,2) has a highly amplified ridge and is associated with warm θ_{e850} over Alaska and the Northwest Territories on the order of 8 K. For all the warm North American Arctic nodes, the geostrophic wind associated with the SLP and 500-hPa height fields are veering with height between the upstream trough and amplified western North American ridge (Fig. 6). This layer mean warm air advection can act to amplify the ridge. Although the SOM was conducted on θ_{e850} anomalies north of 50°N, the node composites show associated cold θ_{e850} anomalies south of 50°N in the northeastern United States, in particular for node (3,2) (Fig. 6). Several of these map nodes are experiencing statistically significant increases in the future, specifically nodes (2,2), (2,3), and (3,2) (Fig. 5).

For the cold North American Arctic nodes, (2,4) has negative θ_{e850} anomalies confined to Alaska/Northwest Territories and resembles the cold Arctic node (3,4), with zonal upper-level flow (Fig. 6) and anomalously low SLP over the Arctic (Fig. 7); however, the negative θ_{e850} anomaly is centered over the continent instead of the central Arctic (Fig. 6). Nodes (1,4) and (3,1) have very cold θ_{e850} anomalies over most of northern North America up to -8 K, with a trough over central North America and ridging upstream over Alaska or the Beaufort/Chukchi Seas (Fig. 6). For each of these, the maximum cold anomaly is located a quarter wavelength upstream of the trough, where you would expect the maximum anticyclonic vorticity advection and cold air advection to occur (Fig. 6). Similar to the warm North American Arctic nodes [(2,2), (2,3), (3,2), and (3,3)] with ridges located over western North America, these patterns are all consistent with a baroclinic wave response over North America (Fig. 6). This is evidenced in the relative locations of the upper-level ridge/trough to the lower-level SLP, where we can see that troughs are tilted westward with height (Fig. 6). Of the cold North American nodes, (1,4) and (2,4) occur at an increased frequency in the future, whereas (3,1) has no significant trend (Fig. 5). This implies a total increase in cold anomalies over the North American Arctic through the period.

The warm eastern Arctic nodes [(1,1), (2,1), and (1,2)] are characterized by positive θ_{e850} anomalies over the eastern or central Arctic and negative anomalies over central Russia or Europe (Fig. 1). Nodes (1,1) and (1,2) have a dipole in SLP anomalies across the eastern Arctic, with a positive anomaly over northern Europe/Russia and negative anomaly over Greenland (Fig. 7). This would favor the southerly advection of warm air from the Atlantic into the eastern Arctic, consistent with the existence of a warm anomaly in the eastern

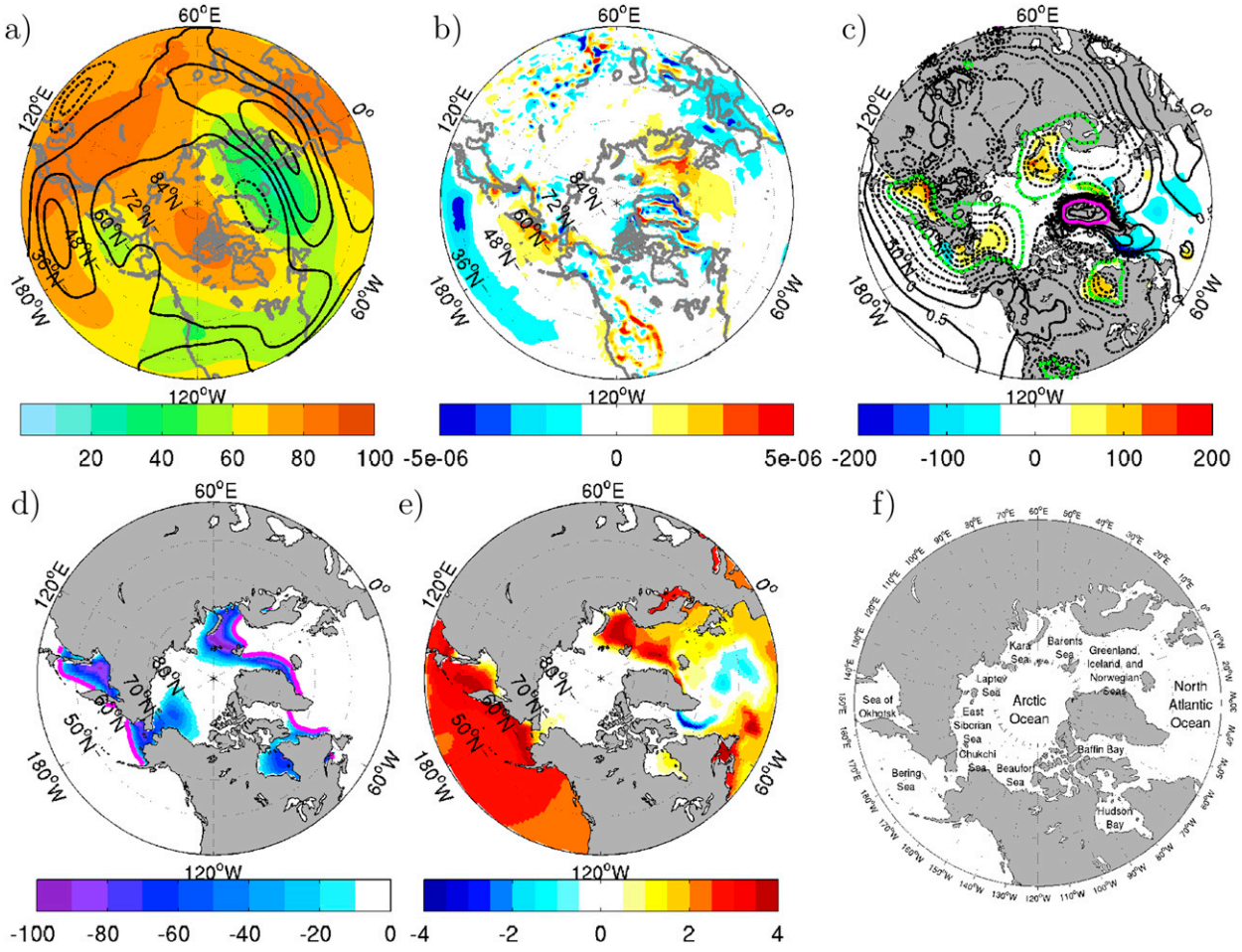

FIG. 4. Decadal JF ensemble-mean difference (2070–80 minus 2010–20) for (a) 500-hPa geopotential height (m; color) and 200-hPa wind speed (contours every 1 m s^{-1}; dashed negative), (b) relative vorticity (s^{-1}), (c) turbulent heat flux (W m^{-2}; color) and SLP (hPa; contoured every 0.5 hPa; dashed negative; −2 hPa in green; and +2 hPa in magenta), (d) SIC (%) with decadal average (2010–20) sea ice edge (magenta line), and (e) SST (K). (f) A map of the Arctic Ocean indicating the locations of peripheral seas.

Arctic (Fig. 6). In the upper levels, these nodes are associated with enhanced ridging in the 500-hPa flow over the Barents and Kara Seas (Fig. 6). Node (2,1) does not have an SLP dipole but rather one large positive SLP anomaly over the entire Arctic (Fig. 7), and the warm anomaly in this pattern is centered over the central Arctic as opposed to nodes (1,1) and (2,1), where it is located more toward the eastern Arctic (Fig. 6). There are significant declines in the frequency of occurrence in nodes (1,1) and (2,1) in the future (Fig. 5).

4. Discussion

In this section, we suggest hypotheses for the causes of trends in the frequency of occurrence of SOM nodes and highlight their relationships to known modes of climate variability. A particular emphasis is placed on climatological changes in surface boundary conditions that may alter planetary-scale circulations associated with these SOM node patterns.

a. Implications for the AO

Node (3,4) is characterized by cold θ_{e850} anomalies over the central Arctic compared to the midlatitudes, lower SLP, and lower 500-hPa geopotential heights (Figs. 6, 7). This node is also experiencing significant declines in the future. The erosion of the Arctic inversion layer may lead to reduced cold air generation over the central Arctic relative to the midlatitudes and be responsible for this change in the frequency of node (3,4).

This pattern is typical of the surface temperature and upper-level exhibition of the positive phase of the AO. The AO is typically defined as the first EOF of SLP over the Arctic, where a positive phase consisting of SLP anomalies that are negative over the central Arctic

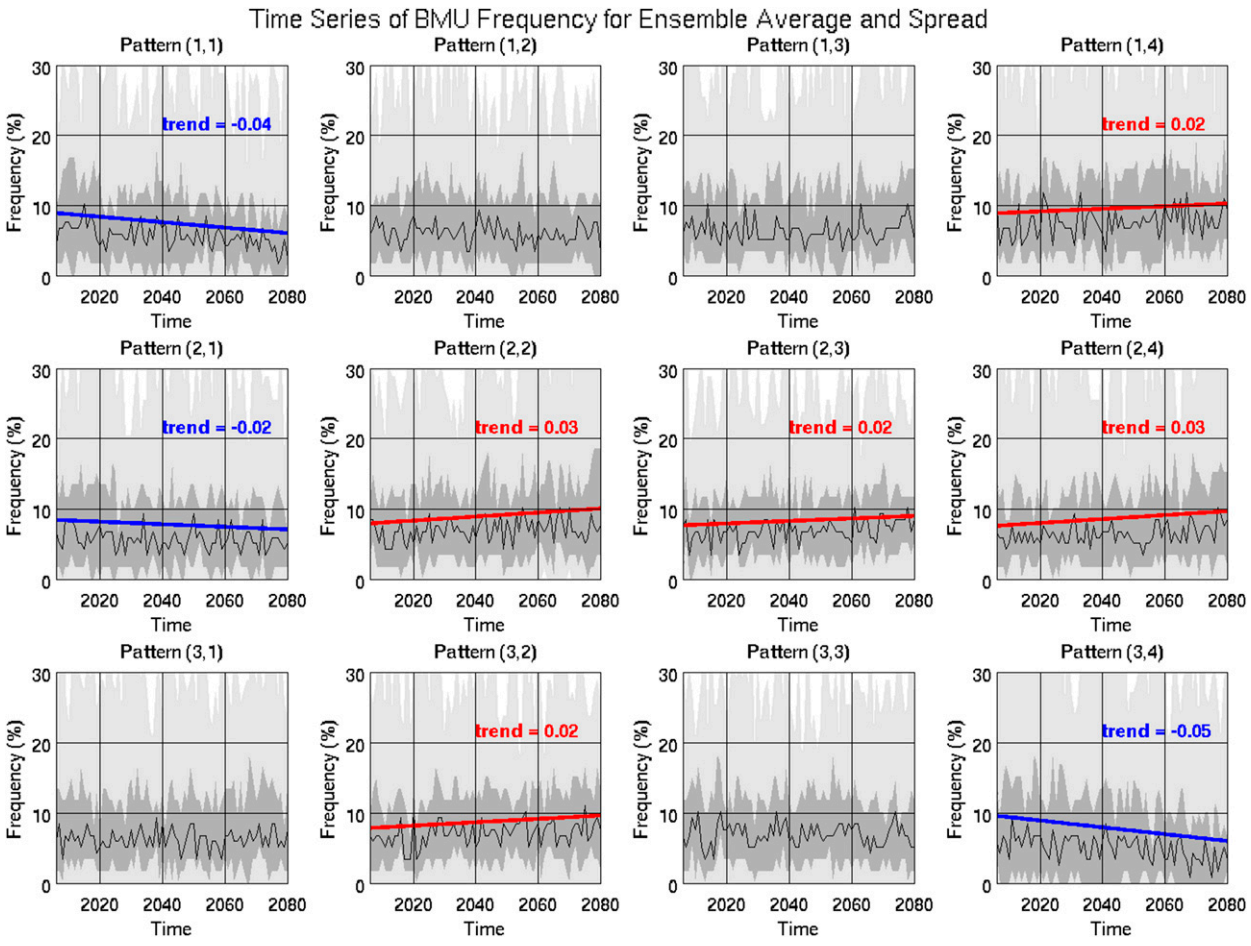

FIG. 5. Ensemble spread in average JF best match unit frequency over time. Ensemble median (solid black line), 25th–75th percentiles (dark gray shading), and maximum to minimum (light gray shading). Statistically significant multiple linear regressions of the best match unit frequencies (at the 95th confidence level) are shown as red (positive) and blue (negative) trend lines with given trend value (% yr^{-1}).

and positive over the North Atlantic and North Pacific (Thompson and Wallace 1998). The AO is generally associated with more zonal upper-level flow, enhanced contrast in upper-level heights between the Arctic and midlatitudes, and a strong polar vortex (Thompson and Wallace 1998).

The airmass pattern in node (3,4) is consistent with the positive phase of the AO; however, the results are not directly comparable to the AO index since the analysis is conducted on θ_{e850}. The results here do suggest some significant airmass changes that could be related to patterns in the large-scale flow. The traditional method of examining such teleconnections uses EOF analysis that requires stationarity in the SLP time series. In the case of global climate change, this assumption is likely invalid. A technique such as self-organizing maps applied to variables that represent the upper- and lower-level manifestations of the AO or NAO could be used to address how these teleconnections may change in the future and how they may be related to airmass generation.

b. *Role of the North Atlantic warming hole*

Amidst the increase in global SST, the North Atlantic has experienced a warming deficit (Drijfhout et al. 2012). This ''North Atlantic warming hole'' has been related to a slowing of the Atlantic meridional overturning circulation (MOC) (Rahmstorf et al. 2015; Drijfhout et al. 2012; Woollings et al. 2012), which is expected to continue to slow in the future (Collins et al. 2013). In the historical period, the MOC has been shown to drive the internal variability of the North Atlantic through its impacts on the Atlantic Multidecadal Oscillation (AMO). Phases of the AMO have, in turn, been related to storm tracks (Yamamoto and Palter 2016), atmospheric circulation patterns (Alexander et al. 2014; Ting et al. 2014), and precipitation (Alexander et al. 2014; Ting et al. 2014) over

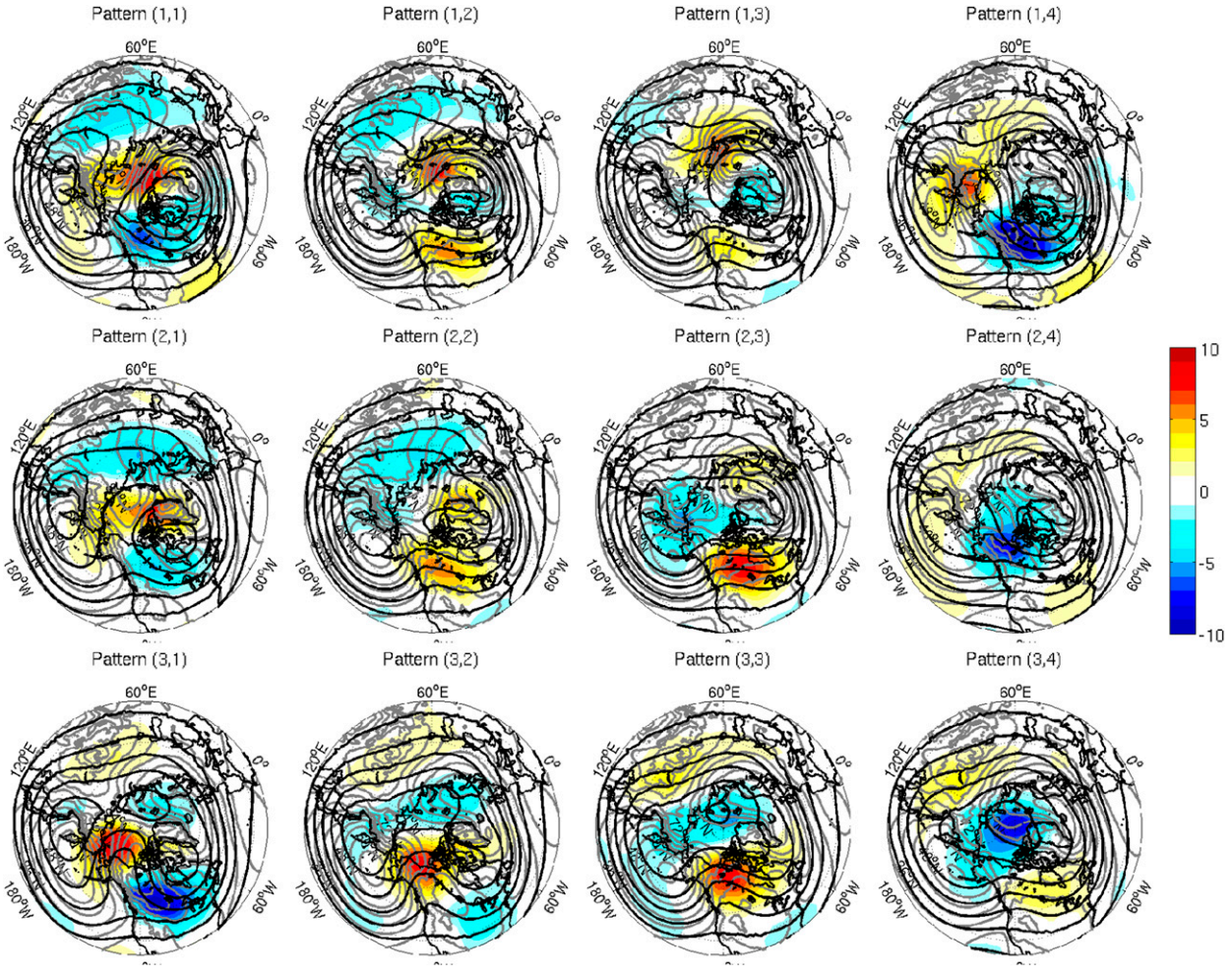

FIG. 6. SOM node (2070–80) equivalent potential temperature anomalies relative to decadal average (K; color), SLP (hPa; gray contours), and geopotential height at 500 hPa (m; black contours).

the North Atlantic. We may therefore expect that the North Atlantic warming hole may have significant consequences for the atmospheric circulation in the future. For example, Woollings et al. (2012) associated the North Atlantic warming hole with an eastward extension of the North Atlantic storm track.

In the CESM-LE, this SST feature is seen in the climatological difference between the 2070–80 and 2010–20 decadal averages, as a region of smaller temperature increase compared to the surroundings (Fig. 4e). The lack of warming extends into the atmosphere, where we can see there is a reduced warming in θ_{e850} (Fig. 3) and consequently lower 500-hPa heights (Fig. 4a), consistent with lower column thicknesses over this region. This results in an enhanced height gradient at 500 hPa in the North Atlantic basin, resulting in a strengthening and extension of the North Atlantic jet. The configuration resembles a shift toward a more positive NAO phase. This is a dynamically consistent mechanism by which changes in the SSTs may be impacting the atmospheric circulations and is consistent with the results of Woollings et al. (2012), indicating an extension of the North Atlantic storm track.

We hypothesize that this climatological forcing decreases the probability of occurrence of nodes (1,1) and (2,1). The strengthening and extension of the jet over Europe shifts the poleward jet exit region over the Barents–Kara Seas. The upper-level forcing of the poleward jet exit region would act to inhibit the formation of the large upper-level ridges over the North Atlantic, typical of nodes (1,1) and (2,1) (Fig. 7). Although there have been suggestions that reduced sea ice in the Barents–Kara Seas would increase the production of anticyclones in the region (Liu et al. 2012; Petoukhov and Semenov 2010), this SST anomaly associated with the North Atlantic warming hole may act to dampen the sea ice signal in the future.

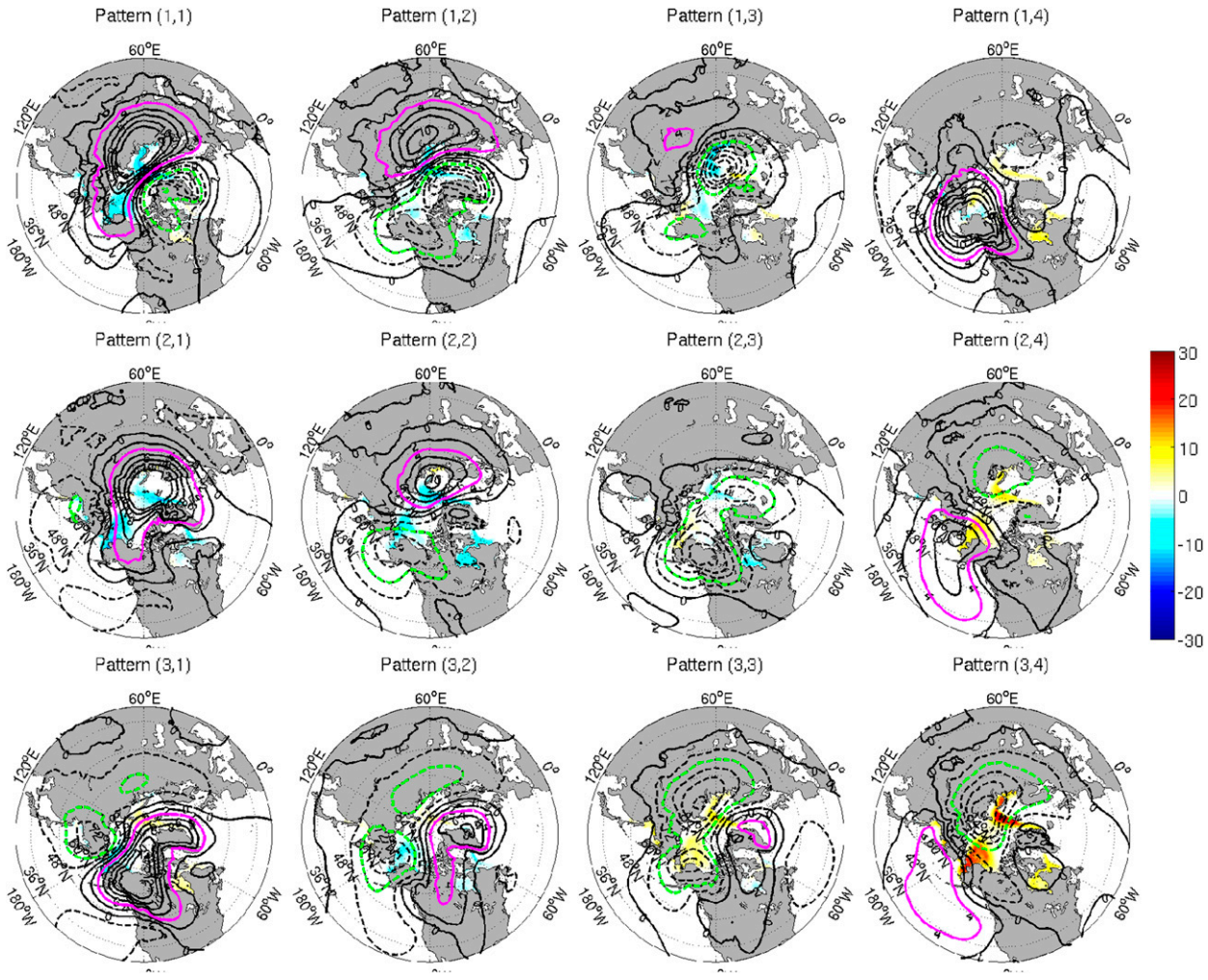

FIG. 7. SOM node anomaly relative to the decadal ensemble average (2070–80) of SIC (%) and SLP (hPa): contoured solid black for positive, dashed black for negative, magenta for +4 hPa, and green for −4 hPa.

c. *Role of sea ice loss*

The presence of sea ice insulates the cold overlying atmosphere from the warmer ocean below. This sea ice cover is declining rapidly, with projections indicating the likelihood of a purely seasonal ice cover prior to the mid-twenty-first century (Collins et al. 2013; Wang and Overland 2012). Although sea ice losses are greatest in the summer, winter sea ice loss has a larger impact on the atmosphere, with greater heat fluxes and consequently larger increases in air temperature (Deser et al. 2010; Singarayer et al. 2006). Several GCM studies have been conducted to study the atmospheric response to sea ice loss using prescribed sea ice and SST boundary conditions that either represent interannual variability in the historical period (Honda et al. 1999; Deser et al. 2000; Alexander et al. 2004; Kvamstøet al. 2004) or future projected sea ice loss (Magnusdottir et al. 2004; Deser et al. 2004; Singarayer et al. 2006; Seierstad and Bader 2009; Deser et al. 2010). A comprehensive review of the topic was conducted by Budikova (2009), although many studies have been published since then. In a twentieth-century GCM modeling study with prescribed sea ice loss from the end of the twenty-first century, Deser et al. (2010) show that sea ice loss in January–February results in an increase in temperature, with the warming concentrated north of 65°N and vertically to 800 hPa and accompanied by an increase in 500-hPa heights over the central Arctic. This mean change is consistent with the declining frequency of pattern (3,4) (Fig. 1), which is characterized by low θ_{e850} and lower geopotential heights over the central Arctic (Fig. 5).

In addition to local impacts on air temperature, many modeling studies have addressed the impact of sea ice loss on the midlatitude flow in the winter (Honda et al.

1999; Deser et al. 2004; Alexander et al. 2004; Magnusdottir et al. 2004; Singarayer et al. 2006; Seierstad and Bader 2009). The midlatitude response to sea ice loss varies depending on the specifics of the experiment, such as region of sea ice loss and month of study. Deser et al. (2004) decomposed the sea ice response to North Atlantic loss into an indirect response that projected onto the NAO and a direct response consisting of the remainder. They found that the indirect response consisted of a negative NAO, and the direct response was a surface low pressure system over the sea ice anomaly and a downstream baroclinic wave. Seierstad and Bader (2009) attributed the incongruities between the responses to North Atlantic sea ice loss in various studies to the amount of indirect versus direct response. Many studies suggest a large indirect response where North Atlantic sea ice loss projects strongly onto the NAO, where low sea ice is related to a negative NAO pattern (Deser et al. 2004; Seierstad and Bader 2009; Alexander et al. 2004; Magnusdottir et al. 2004). Singarayer et al. (2006), however, noted a decrease in sea level pressure over the region of sea ice loss, similar to the direct response of Deser et al. (2004).

Though there are fewer studies that focus on the response to sea ice loss in the western Arctic, the results are consistent. In experiments with prescribed interannual variability in the Sea of Okhotsk, both Honda et al. (1999) and Alexander et al. (2004) found a stationary Rossby wave response to reduced sea ice that extended across the Pacific and into North America. Honda et al. (1999) corroborated these results in the observations looking at differences between high and low sea ice years. In these studies, there is a localized low SLP anomaly above the region of sea ice loss and a downstream ridge in the upper levels (Honda et al. 1999; Alexander et al. 2004), as was found in the direct response of Deser et al. (2004).

We hypothesize that, on a climatological time scale, sea ice reduction may result in the generation of a near-stationary localized thermal low that can provide enhanced forcing to passing upper-level baroclinic waves. Localized maxima in diabatic heating can result in the formation of a surface cyclone (Bluestein 1993, chapter 1). Since sea ice in the Sea of Okhotsk, Bering Sea, and Chukchi Sea is bounded by the land (Fig. 4f), the climatological loss of sea ice and the resulting enhanced turbulent heat fluxes will be localized anomalies. This is seen in the climatological differences between the 2070–80 and 2010–20 ensemble decadal averages, where there is increased turbulent heat fluxes and decreased SLP above regions of sea ice loss (Fig. 4c). The localized low pressure systems (Fig. 4c) and increase in potential vorticity (Fig. 4b) would result in enhanced surface temperature advections. In a dynamically coupled atmosphere, such temperature advections can feed back onto the upper levels through impacts on the height tendencies. As such, a thermal low at the surface could amplify upper-level baroclinic waves passing over the thermal anomaly, provided that it is downstream (upstream) of an upper-level trough (ridge). This is consistent with the direct response to sea ice loss identified by Deser et al. (2004) and the response to anomalous sea ice in the Sea of Okhotsk (Honda et al. 1999; Alexander et al. 2004).

An analogy of this mechanism can be made to the presence of high orography of the Rocky Mountains on the west coast of North America. In the lee of the mountain range, a surface trough is formed as a result of subsidence heating (Bluestein 1993). In addition to generating a climatological surface pressure feature, the presence of the mountains and the lee cyclogenesis associated with them also enhances the development of baroclinic disturbances in the upper levels (Bluestein 1993). In the context of this work, the climatological change in sea ice would be analogous to the development of a region of downsloping, which has an expression as a surface climatological feature and will also impact the development of baroclinic waves.

In the context of the SOM analysis, increased baroclinic wave development resulting from sea ice loss in the western Arctic would be manifested as an increase in the frequency of SOM nodes with an amplified baroclinic ridge over western North America or the western Arctic. This is the case for the warm North American Arctic patterns [(2,2), (2,3), (3,2), and (3,3)] and two of the cold North American Arctic patterns [(1,4) and (3,1)], all of which are associated with amplified 500-hPa flow and consequently have large θ_{e850} anomalies over parts of North America (Fig. 6). All of these patterns are either experiencing no significant change in frequency or a significant increase in frequency (Fig. 5). Over Eurasia, this type of forcing due to sea ice loss also exists; however, we suggest that the existence of a North Atlantic warming hole may be acting to mitigate the effects of sea ice loss in the region.

5. Conclusions

In this study, we apply a technique of self-organizing maps to the new state-of-the-art CESM-LE to identify archetypal Arctic airmass patterns and associated circulation structures that are present through the twenty-first century in the model. We have shown that, in the future, there are changes in the frequency of θ_{e850} anomaly patterns relative to the ensemble-mean climatic change, indicating a change in the internal variability.

In particular, there is a decline in patterns associated with amplified flow over Europe associated with warm θ_{e850} over the eastern Arctic and cold θ_{e850} over central Russia/Europe. These patterns are reminiscent of the cold European winter of 2012/13. Over North America, there is an increase in patterns with more amplified upper-level flow, with an amplified ridge (trough) and positive (negative) θ_{e850} anomalies in western (eastern) North America. The 2014/15 cold winter over eastern North America was similar to the one of these pattern (node (3,2)), which is projected to become more frequent in the future. A pattern with an anomalously cold air mass over the central Arctic, associated with a well-developed polar vortex typical of the positive phase of the Arctic Oscillation, is projected to be less common in the future. These results imply that, during the next century, there may be a transition from a state where cold air is built up over the central Arctic to one in which cold air generation over the North American landmass is more important.

We hypothesize that changes in the surface forcing by sea ice and SSTs could lead to changes in boundary conditions that alter the frequency of occurrence of these patterns. In particular, the change in the frequency of patterns of amplified flow over North America may be related to surface forcing from declining sea ice and resulting enhanced forcing of baroclinic waves. For the Eurasian sector, the existence of a warming hole in SSTs, shown in Drijfhout et al. (2012) to be related to the meridional overturning circulation, may play a role in the decline of this pattern by enhancing the North Atlantic jet. Further research would be required to explore the causality of these mechanisms.

Acknowledgments. Support for this work is provided in part by the Fonds de Recherche en Science du Climat (FRSCO) from the Ouranos Consortium, the Natural Sciences and Engineering Research Council (NSERC) Discovery grants program, the Canadian Sea Ice and Snow Evolution (CanSISE) Network and the Canadian Network for Regional Climate and Weather Prediction funded by the NSERC Climate Change and Atmospheric Research program, and the Fonds de Recherche Nature et Technologies (FRQNT). This work is a contribution to the Department of the Navy, Office of Naval Research, and Québec-Océan. The CESM project is supported by the National Science Foundation and the Office of Science of the U.S. Department of Energy. Computing resources were provided by the NCARs Computational and Information Systems Laboratory (CISL), sponsored by the National Science Foundation and other agencies. We thank Dr. William Gutowski for useful discussions. We would also like to thank Kevin Bowley and three anonymous reviewers for providing useful comments.

REFERENCES

Alexander, M. A., U. S. Bhatt, J. Walsh, M. Timlin, J. Milller, and J. Scott, 2004: The atmospheric response to realistic arctic sea ice anomalies in an AGCM during winter. *J. Climate*, **17**, 890–905, doi:10.1175/1520-0442(2004)017<0890:TARTRA>2.0.CO;2.

——, K. Halimeda Kilbourne, and J. A. Nye, 2014: Climate variability during warm and cold phases of the Atlantic Multidecadal Oscillation (AMO) 1871–2008. *J. Mar. Syst.*, **133**, 14–26, doi:10.1016/j.jmarsys.2013.07.017.

Barton, N. P., S. A. Klein, J. S. Boyle, and Y. Y. Zhang, 2012: Arctic synoptic regimes: Comparing domain-wide Arctic cloud observations with CAM4 and CAM5 during similar dynamics. *J. Geophys. Res.*, **117**, D15205, doi:10.1029/2012JD017589.

Bluestein, H. B., 1993: *Observations and Theory of Weather Systems.* Vol. II, *Synoptic-Dynamic Meteorology in Midlatitudes*, Oxford University Press, 608 pp.

Budikova, D., 2009: Role of Arctic sea ice in global atmospheric circulation: A review. *Global Planet. Change*, **68**, 149–163, doi:10.1016/j.gloplacha.2009.04.001.

Cassano, E. N., A. H. Lynch, J. J. Cassano, and M. R. Koslow, 2006: Classification of synoptic patterns in the western Arctic associated with extreme events at Barrow, Alaska, USA. *Climate Res.*, **30**, 83–97, doi:10.3354/cr030083.

Cassano, J. J., P. Uotila, and A. Lynch, 2006: Changes in synoptic weather patterns in the polar regions in the twentieth and twenty-first centuries, part 1: Arctic. *Int. J. Climatol.*, **26**, 1027–1049, doi:10.1002/joc.1306.

Cavazos, T., 2000: Using self-organizing maps to investigate extreme climate events: An application to wintertime precipitation in the Balkans. *J. Climate*, **13**, 1718–1732, doi:10.1175/1520-0442(2000)013<1718:USOMTI>2.0.CO;2.

Collins, M., and Coauthors, 2013: Long-term climate change: Projections, commitments and irreversibility. *Climate Change 2013: The Physical Science Basis*, T. F. Stocker et al., Eds., Cambridge University Press, 1029–1136, doi:10.1017/CBO9781107415324.024.

Curry, J., 1983: On the formation of continental polar air. *J. Atmos. Sci.*, **40**, 2278–2292, doi:10.1175/1520-0469(1983)040<2278:OTFOCP>2.0.CO;2.

De Boer, G., W. Chapman, J. E. Kay, B. Medeiros, M. D. Shupe, S. Vavrus, and J. Walsh, 2012: A characterization of the present-day arctic atmosphere in CCSM4. *J. Climate*, **25**, 2676–2695, doi:10.1175/JCLI-D-11-00228.1.

DeRepentigny, P., B. Tremblay, R. Newton, and S. Pfirman, 2015: Patterns of sea-ice retreat in the transition to a seasonally ice-free arctic. *J. Climate*, submitted.

Deser, C., J. Walsh, and M. Timlin, 2000: Arctic sea ice variability in the context of recent atmospheric circulation trends. *J. Climate*, **13**, 617–633, doi:10.1175/1520-0442(2000)013<0617:ASIVIT>2.0.CO;2.

——, G. Magnusdottir, R. Saravanan, and A. Phillips, 2004: The effects of North Atlantic SST and sea ice anomalies on the winter circulation in CCM3. Part II: Direct and indirect components of the response. *J. Climate*, **17**, 877–889, doi:10.1175/1520-0442(2004)017<0877:TEONAS>2.0.CO;2.

——, R. Tomas, M. Alexander, and D. Lawrence, 2010: The seasonal atmospheric response to projected arctic sea ice loss in the late twenty-first century. *J. Climate*, **23**, 333–351, doi:10.1175/2009JCLI3053.1.

Drijfhout, S., G. J. van Oldenborgh, and A. Cimatoribus, 2012: Is a decline of AMOC causing the warming hole above the North Atlantic in observed and modeled warming patterns? *J. Climate*, **25**, 8373–8379, doi:10.1175/JCLI-D-12-00490.1.

Gent, P. R., and Coauthors, 2011: The Community Climate System Model version 4. *J. Climate*, **24**, 4973–4991, doi:10.1175/2011JCLI4083.1.

Graversen, R., P. Langen, and T. Mauritsen, 2014: Polar amplification in CCSM4: Contributions from the lapse rate and surface albedo feedbacks. *J. Climate*, **27**, 4433–4450, doi:10.1175/JCLI-D-13-00551.1.

Hewitson, B. C., and R. G. Crane, 2002: Self-organizing maps: Applications to synoptic climatology. *Climate Res.*, **22**, 13–26, doi:10.3354/cr022013.

Holland, M. M., and C. M. Bitz, 2003: Polar amplification of climate change in coupled models. *Climate Dyn.*, **21**, 221–232, doi:10.1007/s00382-003-0332-6.

Holton, J., 2004: *An Introduction to Dynamic Meteorology*. 4th ed. International Geophysics Series, Vol. 88, Elsevier Inc., 535 pp.

Honda, M., K. Yamazaki, H. Nakamura, and K. Takeuchi, 1999: Dynamic and thermodynamic characteristics of atmospheric response to anomalous sea-ice extent in the Sea of Okhotsk. *J. Climate*, **12**, 3347–3358, doi:10.1175/1520-0442(1999)012<3347:DATCOA>2.0.CO;2.

Hurrell, J. W., and Coauthors, 2013: The Community Earth System Model: A framework for collaborative research. *Bull. Amer. Meteor. Soc.*, **94**, 1339–1360, doi:10.1175/BAMS-D-12-00121.1.

Huth, R., C. Beck, A. Philipp, M. Demuzere, Z. Ustrnul, M. Cahynová, J. Kyselý, and O. E. Tveito, 2008: Classifications of atmospheric circulation patterns: Recent advances and applications. *Ann. N. Y. Acad. Sci.*, **1146**, 105–152, doi:10.1196/annals.1446.019.

Jahn, A., and Coauthors, 2012: Late-twentieth-century simulation of arctic sea ice and ocean properties in the CCSM4. *J. Climate*, **25**, 1431–1452, doi:10.1175/JCLI-D-11-00201.1.

Johnson, N. C., S. B. Feldstein, and B. Tremblay, 2008: The continuum of Northern Hemisphere teleconnection patterns and a description of the NAO shift with the use of self-organizing maps. *J. Climate*, **21**, 6354–6371, doi:10.1175/2008JCLI2380.1.

Kay, J. E., M. M. Holland, C. M. Bitz, E. Blanchard-Wrigglesworth, A. Gettelman, A. Conley, and D. Bailey, 2012: The influence of local feedbacks and northward heat transport on the equilibrium Arctic climate response to increased greenhouse gas forcing. *J. Climate*, **25**, 5433–5450, doi:10.1175/JCLI-D-11-00622.1.

——, and Coauthors, 2014: The Community Earth System Model (CESM) Large Ensemble project: A community research for studying climate change in the presence of internal climate variability. *Bull. Amer. Meteor. Soc.*, **96**, 1333–1349, doi:10.1175/BAMS-D-13-00255.

Kohonen, T., 1982: Self-organized formation of topologically correct feature maps. *Biol. Cybern.*, **43**, 59–69, doi:10.1007/BF00337288.

——, 2001: *Self-Organizing Maps*. 3rd ed. Springer Series in Information Sciences, Vol. 30, Springer, 502 pp.

Kvamstø, N. G., P. Skeie, and D. B. Stephenson, 2004: Impact of Labrador sea-ice extent on the North Atlantic oscillation. *Int. J. Climatol.*, **24**, 603–612, doi:10.1002/joc.1015.

Liu, J., J. A. Curry, H. Wang, M. Song, and R. M. Horton, 2012: Impact of declining Arctic sea ice on winter snowfall. *Proc. Natl. Acad. Sci. USA*, **109**, 4047–4079, doi:10.1073/pnas.1114910109.

Liu, Y., R. H. Weisberg, and C. N. K. Mooers, 2006: Performance evaluation of the self-organizing map for feature extraction. *J. Geophys. Res.*, **111**, C05018, doi:10.1029/2005JC003117.

Magnusdottir, G., C. Deser, and R. Saravanan, 2004: The effects of North Atlantic SST and sea ice anomalies on the winter circulation in CCM3. Part I: Main features and storm track characteristics of the response. *J. Climate*, **17**, 857–876, doi:10.1175/1520-0442(2004)017<0857:TEONAS>2.0.CO;2.

Manabe, S., and R. Wetherald, 1975: The effects of doubling the CO_2 concentration on the climate of a general circulation model. *J. Atmos. Sci.*, **32**, 3–15, doi:10.1175/1520-0469(1975)032<0003:TEODTC>2.0.CO;2.

Murtagh, F., and M. Hernández-Pajares, 1995: The Kohonen self-organizing map method: An assessment. *J. Classif.*, **12**, 165–190, doi:10.1007/BF03040854.

Neale, R. B., and Coauthors, 2012: Description of the NCAR Community Atmosphere Model (CAM 5.0). NCAR Tech. Note NCAR/TN-486+STR, 283 pp. [Available online at http://www.cesm.ucar.edu/models/cesm1.0/cam/docs/description/cam5_desc.pdf.]

Petoukhov, V., and V. A. Semenov, 2010: A link between reduced Barents–Kara sea ice and cold winter extremes over northern continents. *J. Geophys. Res.*, **115**, D21111, doi:10.1029/2009JD013568.

Pithan, F., and T. Mauritsen, 2014: Arctic amplification dominated by temperature feedbacks in contemporary climate models. *Nat. Geosci.*, **7**, 181–184, doi:10.1038/ngeo2071.

Rahmstorf, S., J. E. Box, G. Feulner, M. E. Mann, A. Robinson, S. Rutherford, and E. J. Schaffernicht, 2015: Exceptional twentieth-century slowdown in Atlantic Ocean overturning circulation. *Nat. Climate Change*, **5**, 475–480, doi:10.1038/nclimate2554.

Reusch, D. B., R. B. Alley, and B. C. Hewitson, 2005: Relative performance of self-organizing maps and principal component analysis in pattern extraction from synthetic climatological data. *Polar Geogr.*, **29**, 188–212, doi:10.1080/789610199.

——, ——, and ——, 2007: North Atlantic climate variability from a self-organizing map perspective. *J. Geophys. Res.*, **112**, D02104, doi:10.1029/2006JD007460.

Sammon, J., 1969: A nonlinear mapping for data structure analysis. *IEEE Trans. Comput.*, **18**, 401–409, doi:10.1109/T-C.1969.222678.

Schuenemann, K. C., and J. J. Cassano, 2009: Changes in synoptic weather patterns and Greenland precipitation in the 20th and 21st centuries: 1. Evaluation of late 20th century simulations from IPCC models. *J. Geophys. Res.*, **114**, D20113, doi:10.1029/2009JD011705.

——, and ——, 2010: Changes in synoptic weather patterns and Greenland precipitation in the 20th and 21st centuries: 2. Analysis of 21st century atmospheric changes using self-organizing maps. *J. Geophys. Res.*, **115**, D05108, doi:10.1029/2009JD011706.

Screen, J., and I. Simmonds, 2010: The central role of diminishing sea ice in recent Arctic temperature amplification. *Nature*, **464**, 1334–1337, doi:10.1038/nature09051.

Seierstad, I. A., and J. Bader, 2009: Impact of a projected future Arctic Sea Ice reduction on extratropical storminess and the NAO. *Climate Dyn.*, **33**, 937–943, doi:10.1007/s00382-008-0463-x.

Serreze, M. C., A. P. Barrett, J. C. Stroeve, D. N. Kindig, and M. M. Holland, 2008: The emergence of surface-based Arctic amplification. *Cryosphere Discuss.*, **2**, 601–622, doi:10.5194/tcd-2-601-2008.

Simpson, I. R., T. A. Shaw, and R. Seager, 2014: A diagnosis of the seasonally and longitudinally varying midlatitude circulation response to global warming. *J. Atmos. Sci.*, **71**, 2489–2515, doi:10.1175/JAS-D-13-0325.1.

Singarayer, J., J. Bambier, and P. Valdes, 2006: Twenty-first-century climate impacts from a declining Arctic sea ice cover. *J. Climate*, **19**, 1109–1125, doi:10.1175/JCLI3649.1.

Thompson, D. W. J., and J. M. Wallace, 1998: The Arctic oscillation signature in the wintertime geopotential height and temperature fields. *Geophys. Res. Lett.*, **25**, 1297–1300, doi:10.1029/98GL00950.

Ting, M., Y. Kushnir, and C. Li, 2014: North Atlantic Multidecadal SST Oscillation: External forcing versus internal variability. *J. Mar. Syst.*, **133**, 27–38, doi:10.1016/j.jmarsys.2013.07.006.

Tremblay, L., 2001: Can we consider the Arctic Oscillation independently from the Barents Oscillation? *Geophys. Res. Lett.*, **28**, 4227–4230, doi:10.1029/2001GL013740.

Vesanto, J., J. Himberg, E. Alhoniemi, and J. Parhankangas, 2000: SOM toolbox for Matlab 5. Helsinki University of Technology Tech. Rep. A57, 60 pp.

Walsh, J. E., A. S. Phillips, D. H. Portis, and W. L. Chapman, 2001: Extreme cold outbreaks in the United States and Europe, 1948–99. *J. Climate*, **14**, 2642–2658, doi:10.1175/1520-0442(2001)014<2642:ECOITU>2.0.CO;2.

Wang, M., and J. E. Overland, 2012: A sea ice free summer Arctic within 30 years: An update from CMIP5 models. *Geophys. Res. Lett.*, **39**, L18501, doi:10.1029/2012GL052868.

Woollings, T., J. Gregory, J. Pinto, M. Reyers, and D. Brayshaw, 2012: Response of the North Atlantic storm track to climate change shaped by ocean–atmosphere coupling. *Nat. Geosci.*, **5**, 313–317, doi:10.1038/ngeo1438.

Yamamoto, A., and J. Palter, 2016: The absence of an Atlantic imprint on the multidecadal variability of wintertime European temperature. *Nat. Commun.*, doi:10.1038/ncomms10930, in press.